Supplementary Information for "Exceptional eruptive CO_2 emissions from intra-plate alkaline magmatism in the Canary volcanic archipelago" by Burton et al., 2023

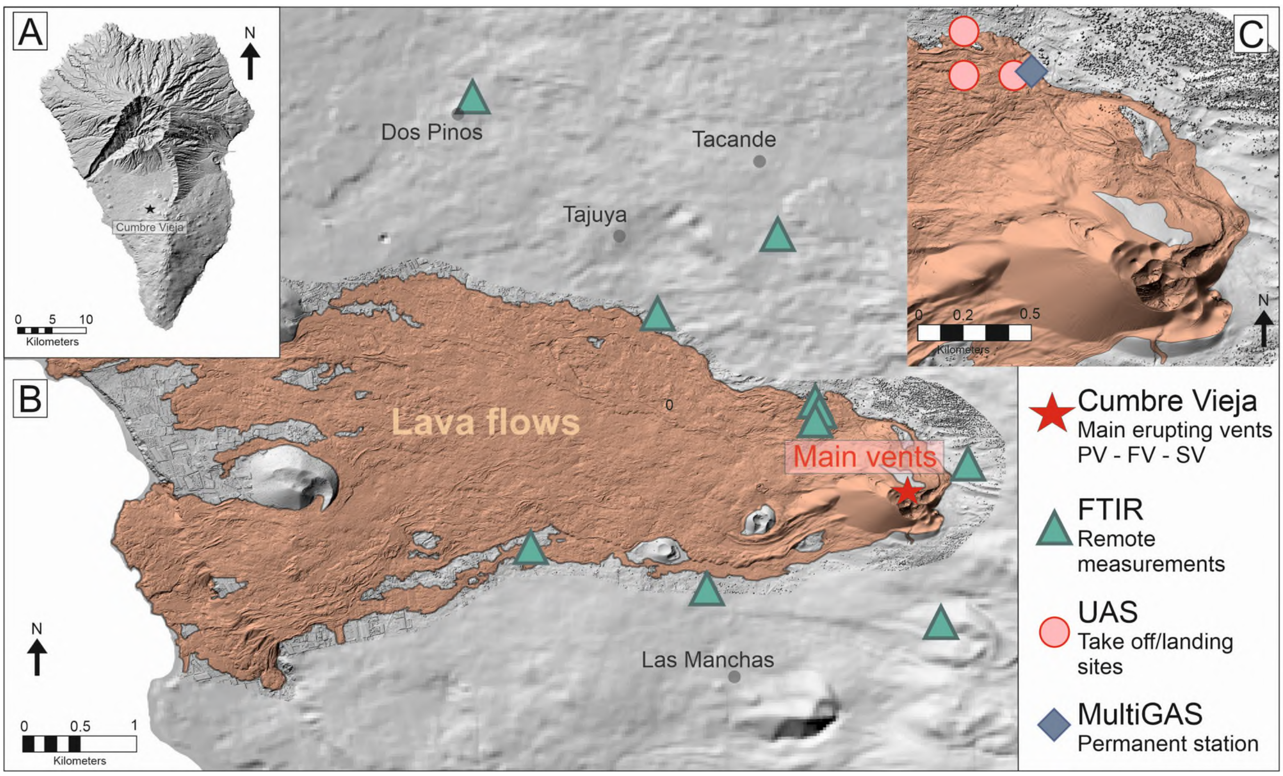

Supplementary Figure 1: (a) Relief map of the island of La Palma; (b) map of the eruptive site, showing lava flows in orange and blue triangles for the location of gas sampling; (c) detail of the near vent sampling area

Supplementary Table 1: CO_2/SO_2 molar ratios measured with MultiGas and FTIR during the 2021 eruption of Tajogaite, La Palma, Canary Islands

Method	Date	Time UTC	Measurement Site	Vent Type	activity type	CO_2/SO_2
Multi-GAS	01/10/2021	10:00	Gas composition measured by aerial multigas from lateral vent on northern flank	EV	lateral effusive vent	0.3
Multi-GAS	02/10/2021	11:30	Gas composition measured by aerial multigas from lateral vent on northern flank	EV	lateral effusive vent	0.04
Multi-GAS	04/10/2021	11:15	Gas composition measured by aerial multigas above the upper effusive vent	EV	main effusive vent	0.07
Multi-GAS	30/09/2021	09:00	Gas composition measured by ground-based portable multi-gas in the downwind grounding plume of the lava fountaining, taken about ~900m from the main cone.	FV	lava fountaining	52

Multi-GAS	01/10/2021	02:00	Gas composition measured by ground-based fixed multi-gas in the downwind grounding plume of the lava fountaining, taken about ~900m from the main cone.	FV	lava fountaining	25
Multi-GAS	01/10/2021	05:00	Gas composition measured by ground-based fixed multi-gas in the downwind grounding plume of the lava fountaining, taken about ~900m from the main cone	FV	lava fountaining	46
Multi-GAS	27/09/2021	16:30	Gas composition measured by aerial multigas above the rim of the main cone. The measurements were acquired during a period of eruptive quiescence before explosive activity resumed approximately 30 minutes later.	PV	quiescently degassing vent	6.8
Multi-GAS	30/09/2021	09:00	Gas composition measured by ground-based fixed multi-gas in the downwind grounding plume of the spattering vent taken about ~900m from the main cone	SV	spattering vent	16
Multi-GAS	01/10/2021	02:00	Gas composition measured by ground-based fixed multi-gas in the downwind grounding plume of the spattering vent taken about ~900m from the main cone	SV	spattering vent	13
Multi-GAS	01/10/2021	05:00	Gas composition measured by ground-based fixed multi-gas in the downwind grounding plume of the spattering vent taken about ~900m from the main cone	SV	spattering vent	6.2
Multi-GAS	01/10/2021	06:00	Gas composition measured by ground-based fixed multi-gas in the downwind grounding plume of the spattering vent taken about ~900m from the main cone	SV	spattering vent	2.8
Multi-GAS	01/10/2021	07:00	Gas composition measured by ground-based fixed multi-gas in the downwind grounding plume of the spattering vent taken about ~900m from the main cone	SV	spattering vent	2.7
Multi-GAS	01/10/2021	08:00	Gas composition measured by ground-based fixed multi-gas in the downwind grounding plume of the spattering vent taken about ~900m from the main cone	SV	spattering vent	2.8

Multi-GAS	03/10/2021	11:00	Gas composition measured by aerial multi-gas in the plume from the spattering vent on the northern flank.	SV	spattering vent	2.8
OP-FTIR	03/10/2021	14:21	Tacande house 28.635N, 17.877W	FV	main ash column	16.3
OP-FTIR	03/10/2021	15:12	Tacande house 28.635N, 17.877W	FV	main ash column	14.1
OP-FTIR	03/10/2021	15:39	Tacande house 28.635N, 17.877W	FV	main ash column	24.1
OP-FTIR	03/10/2021	16:15	Tacande house 28.635N, 17.877W	FV	main ash column	33.6
OP-FTIR	03/10/2021	16:25	Tacande house 28.635N, 17.877W	FV	main ash column	30.3
OP-FTIR	16/10/2021		Tajuya	FV	base of lava fountain	29
OP-FTIR	17/10/2021		Paraiso	FV	base of lava fountain	34
OP-FTIR	31/10/2021		Las Manchas 28.610N, 17.896W	FV	base of lava fountain	37
OP-FTIR	06/11/2021	21:00	Dos Pinos Involcan Base 28.646N, 17.901W	FV	vigorous strombolian activity at main vent	33.5
OP-FTIR	23/11/2021		Base	FV	base of lava fountain	38.3
OP-FTIR	25/11/2021		Tacande	FV	base of lava fountain	38
OP-FTIR	02/12/2021	18:25	Cabeza de Vaca 2 28.617N, 17.862W	FV	lava fountaining at NE vent	35.8
OP-FTIR	03/12/2021		Cabeza de Vaca 2 28.617N, 17.862W	FV	base of lava fountain	35.8
OP-FTIR	03/10/2021	14:30	Tacande flow 28.622N, 17.874W	SV	spattering vent	10.8
OP-FTIR	03/10/2021		Tacande_middleVent_INGV	SV	spattering vent	5
OP-FTIR	03/10/2021		Tacande spattering_INGV	SV	spattering vent	11
OP-FTIR	03/10/2021		Villa UK	SV	spattering vent	8
OP-FTIR	05/10/2021		Tacande	SV	spattering vent	4
OP-FTIR	05/10/2021		Tacande 4coadds	SV	spattering vent	6
OP-FTIR	07/10/2021		Tajuya mid_vent	SV	spattering of vent of lava flow	4
OP-FTIR	07/10/2021		Tajuya low vent	SV	spattering of vent of lava flow	9
OP-FTIR	07/10/2021		Tajuya	SV	spattering vent	13
OP-FTIR	13/10/2021		Tacande	SV	spattering vent	11

OP-FTIR	13/10/2021		Tajuya rotonda	SV	spattering vent	9
OP-FTIR	14/10/2021		Tacande	SV	spattering vent	7
OP-FTIR	25/11/2021		base lava fountain	SV	base of lava fountain	2.9
OP-FTIR	04/12/2021	19:30	Las Manchas 28.610N, 17.896W	SV	spattering of vent of lava flow	9.3
OP-FTIR	05/12/2021	13:30	Las Manchas 28.610N, 17.896W	SV	vent of lava flow	5.3

Silicate melt inclusions from the 2021 Cumbre Vieja eruption: Samples, methods, results

Samples

Fresh samples of magmatic tephra were obtained from fall deposits of known eruption date (**Supplementary Table 2**). Bulk tephra samples consist of fine to medium lapilli; glassy shards; angular lithic clasts; and loose crystals of clinopyroxene, olivine and amphibole. Samples from site M8 were collected on 1 October near the Mirador Astronomico Llano del Jable, located 1.4 km from the vent. At this site the deposit was 17.5 cm thick and comprised a basal 12 cm-thick layer of fine lapilli (A); two intermediate layers of fine to medium vesicular lapilli (B, C) totalling 4.5 cm; and an upper 1 cm of fine black lapilli (D). Samples M8 A-D correspond to the fissure opening phase and the first week of the eruption, when activity consisted of alternating lava fountains, rapid Strombolian explosions, and sporadic Hawaiian fountains (Romero et al., 2022); 'a'ā lava flows drained to the west from the topographically lower vents simultaneously with explosive activity from the upper vents. Later in the eruption, samples CAN-TLP were produced during Strombolian activity, intermittent lava fountaining, and gas jetting events that, after 11 October, interplayed with ash-laden Strombolian columns (Romero et al., 2022).

Supplementary Table 2: Eruption dates and collection locations of tephra samples from the 2021 Cumbre Vieja eruption used in this study.

Sample	Collection location	Eruption date
M8-A	28.61705° N 17.85253° W	19-20 September 2021
M8-C	28.61705° N 17.85253° W	23-25 September 2021
M8-D	28.61705° N 17.85253° W	26 September 2021
CAN-TLP-0037	28.62533° N 17.88546° W	04 October 2021
LPA-16	28.62291° N 17.87372° W	04 October 2021
CAN-TLP-0039	28.60138° N 17.88822° W	05 October 2021
CAN-TLP-0040	28.60652° N 17.88285° W	05 October 2021
CAN-TLP-0042	28.60652° N 17.88285° W	06 October 2021
CAN-TLP-0052	28.61712° N 17.84926° W	08 October 2021
CAN-TLP-0053	28.61712° N 17.84926° W	08 October 2021
CAN-TLP-0128	28.60652° N 17.88285° W	19 October 2021
CAN-TLP-0168	28.60652° N 17.88285° W	29 October 2021

Olivine macrocrysts in the tephra samples (≤1 modal %; Pankhurst et al., 2022) are euhedral to anhedral isolated crystals, equant to sub-equant, and typically fall in the size range 500-1000 µm. The largest crystal measured was 1.7×1.3 mm. The majority of crystals inspected were optically unzoned and devoid of inclusions. Five to ten percent of olivines contain micron-scale oxide inclusions, carbonic fluid inclusions, and/or a small number of silicate melt inclusions or embayments. Rare anhedral and almost opaque olivines are saturated with trails of carbonic fluid inclusions that intersect in different directions, and oxides. These crystals are thought to be antecrysts or xenocrysts entrained from wall rock or from deeper within the magmatic system.

This study focused on glassy silicate melt inclusions and embayments hosted in olivine. Few melt inclusions have a regular elliptical shape, while many have irregular geometries reflecting the necking down of an embayment. Many inclusions contain trapped oxides, sulfides or other silicate mineral phases, and/or one or more vapour bubbles. The melt inclusions selected for analysis were texturally isolated or in reduced clusters; glassy with no daughter crystals; located away from fractures; and showed no visual evidence of decrepitation. Most of the analysed inclusions contained a fluid bubble that occupied an average 2.5% of the total inclusion volume, where inclusion and bubble dimensions were measured by analysis of optical microscope images. The volume ratio between the bubble and the melt inclusion V_b/V_m is between 0.013 and 0.034, which suggests that >75% of the original trapped CO_2 in the inclusion may have diffused into the bubble upon cooling (Moore et al., 2015; Wallace et al., 2015) (**Supplementary Table 3**).

Glassy shards from fragmented lapilli are highly vesicular and contain tiny acicular plagioclases and clinopyroxenes and euhedral oxides scattered in the groundmass.

Supplementary Table 3: Dimensions of melt inclusions and fluid bubbles analysed for volatile contents by Raman and FTIR spectroscopy.

Olivine crystal	**Host olivine dimensions, µm**	**Melt inclusion volume V_m, µm³**	**Fluid bubble volume V_b, µm³**	**V_b/V_m**
CAN-TLP-0037-ol1	1500 × 1000	13222	394	0.023
CAN-TLP-0037-ol3	1000 × 500	7721	265	0.034
CAN-TLP-0039-ol1	1700 × 1300	23204	359	0.015
CAN-TLP-0040-ol2	1500 × 1000	17391	230	0.013
CAN-TLP-0040-ol4	1100 × 1000	14001	286	0.020
CAN-TLP-0052-ol2	1500 × 1500	156321	3739	0.024

1. Analytical methods

We measured the major element compositions of glassy inclusions, embayments, and their host crystals by electron probe microanalysis (EPMA) at the University of Bristol, UK, and the Laboratoire Magmas et Volcans (LMV), Clermont Ferrand, France. Further analyses of melt inclusion volatile contents were conducted on a subset of melt inclusions at LMV. Below we describe the analytical methods employed at both laboratories.

1.1. Laboratoire Magmas et Volcans (LMV), Clermont Ferrand, France

Sample preparation

Olivine crystals in the size range 500-1500 µm were hand-picked from crushed, sieved bulk tephra samples with the aid of a binocular microscope, yielding a total of ~700 olivines. Crystals wrapped by a thin glassy film were cleaned in weak (15%) hot HF for 30 minutes. Cleaned crystals were doubly polished and examined under optical microscope for the presence of melt inclusions. Twenty-five crystals containing glassy melt inclusions measuring >25 μm across were selected for further study. These target inclusions were prepared for analysis by Raman spectroscopy by further polishing to reduce the distance between the fluid bubble and the sample surface to a maximum 30 μm. Glassy shards of vesicular tephra were picked under binocular microscope and doubly polished for analysis.

Raman spectroscopy

Inclusion-hosted bubbles were analyzed at LMV using a Renishaw inVia confocal micro-Raman spectrometer equipped with a 532 nm diode laser (200 mW output power), a Rayleigh rejection edge filter, a 1024×256 pixel CCD detector, and a Leica DM 2500M optical microscope with a motorized XYZ stage. Raman spectra were collected in backscattered geometry, using a 2400 grooves/mm grating, a high confocality setting (i.e., 20 μm slit aperture) and a 100× microscope objective. The applied laser power varied between 5 and 20 mW. WiRE™ 4.4 software was used to acquire and process the spectra. One to four acquisitions of 30 s each were acquired in each bubble. The spectra were recorded in the ~200-1450 cm^{-1} range, which includes the CO_2 Fermi diad peaks at ~1284 and ~1387 cm^{-1} and the main carbonate peaks near 1090 cm^{-1}. For daily calibration of the spectrometer, we carried out repeat measurements of Neon atomic lines and of diamond (peak centred at 1331.5 cm^{-1}), under the same operating conditions as the unknowns.

Spectra were processed by removing a polynomial baseline determined by an in-built fitting algorithm. The two CO_2 peaks were fitted with a Gaussian-Lorentzian mixed profile using WiRE™ 4.4 software. To check the reproducibility, two standard CO_2 fluid inclusions were measured repeatedly during each session. The fluid density of the analyzed inclusion-hosted bubbles was calculated based on the CO_2 densimeter of Song et al. (2009).

Fourier Transform Infrared spectroscopy (FTIR)

Following Raman analyses, the three largest melt inclusions were prepared as doubly exposed polished wafers for analysis by Fourier Transform Infrared Spectroscopy (FTIR). Doubly polished wafers of glassy tephra shards were also prepared for analysis by FTIR. For the doubly polished samples, FTIR was conducted before EPMA in order to avoid beam damage and minimize volatile loss.

Carbon and water concentrations in glasses were measured at LMV by FTIR spectroscopy, using a Bruker Vertex 70 spectrometer coupled with a Hyperion microscope system and equipped with a globar light source, a KBr beam splitter, and a Mercury-Cadmium-Tellurium (MCT) alloy detector. Glass spectra were recorded using the OPUS software in the 700-7500 cm^{-1} range. For the absorbance and background spectra, 600 and 200 scans were acquired, respectively. Species concentrations C (wt.%) were calculated according to the Beer-Lambert law:

$$C = \frac{100 \cdot A \cdot M}{\varepsilon \cdot \rho \cdot t}$$

where A is the absorbance, M the molar mass ($g \cdot mol^{-1}$), ε the molar absorptivity ($L \cdot mol^{-1} \cdot cm^{-1}$), t the thickness measured under an optical microscope (cm), and ρ the glass density ($g \cdot cm^{-3}$) calculated following Lange and Carmichael (1990). Total dissolved water (H_2O_{mol} + OH^-) concentrations were derived from the intensity of the broad band at 3535 cm^{-1} using the molar absorption coefficient of 57.3 ± 1.8 $L \cdot mol^{-1} \cdot cm^{-1}$ (Shishkina et al., 2014). CO_2 concentrations were determined from the height of the peak at 1520 cm^{-1} on the background-subtracted spectra. We calculated the molar absorption coefficient according to the following equation (Dixon and Pan, 1995):

$$\varepsilon_{1520} = 451 - 342\left(\frac{Na}{Ca + Na}\right)$$

Estimated relative errors are <10% for H_2O and 15% for CO_2.

Electron probe microanalysis (EPMA)

Major element compositions of silicate groundmass glass, melt inclusions and their host olivines were measured using a Cameca SXFive instrument. Glass analyses were performed using a 10 nA defocused beam with beam diameter 10 µm), and counting times varying from 10 to 25 s. Concentrations of S, Cl and P were determined in a second analytical condition using a 30 nA defocused beam with beam diameter 15 µm and on-peak counting times of 240 s. Precision and accuracy were assessed by repeat analyses of international standard VG-2. Relative errors are <4% for Cl at concentration levels of 250 µg/g, <3% for S, <6% for P, <5% for K_2O, and <3% for all the other major elements.

Compositions of host olivine crystals were obtained using a 20 nA focused beam at 15 keV, with on-peak counting times from 10 to 20 s. Three spots were made surrounding each melt inclusion, and averaged to obtain the host olivine composition. Precision and accuracy were assessed by repeat analyses of the San Carlos Olivine and the Puy de Dôme Clinopyroxene international standards. Relative errors are <6.5% for Ni and Mn, <5% for Fe and Ca, and <1% for Si and Mg.

1.2. Analytical methods: University of Bristol

Sample preparation

Olivine crystals in the size range 500-1000 µm were hand-picked from crushed, sieved bulk tephra samples with the aid of a binocular microscope. Crystals were cleaned in acetone, mounted in epoxy, and polished to expose melt inclusions and embayments for analysis.

Electron probe microanalysis (EPMA)

Major element compositions of silicate groundmass glass, embayments, melt inclusions and their host olivines were measured using a Cameca SX100 instrument at the University of Bristol, UK. The instrument was calibrated using the following primary standards: albite for Si and Na; rutile for Ti; sanidine for Al and K; haematite for Fe; pure metal for Mn; forsterite for Mg; wollastonite for Ca; apatite for P; Cr_2O_3 for Cr; barite for S; MgF_2 for F; halite for Cl. Glass analyses were performed using an operating potential of 15 kV and beam diameter 5 µm; major elements (Si, Al, Fe, Ca, Na, K, P) were measured with a 10 nA beam current while volatile and selected major and minor elements (S, F, Cl, Ti, Mn, Mg, Cr) were measured under a second condition at 40 nA. Mineral analyses were performed using an operating potential of 15 kV, beam diameter 5 µm, and 10 nA beam current. Sodium was always measured first to minimise loss by volatilization. All elements were measured in WDS mode with peak counting times between 10 and 120 s depending on element abundance. Background count times were half the peak count times. Internal data reduction was performed using PAP matrix corrections for all analyses. Precision and accuracy were assessed by repeat analyses of international basalt glass standards BCR2-G and VG-2, St John's Island olivine, and a diopside standard. 1σ precision estimates are <1% for Si, Al, Fe, Mg; <2% for Ti, Ca; <5% for Mn, Na, K; <8% for P; <2% for S at concentration levels of 1500 µg/g; <8% for Cl and ~30% for F at concentration levels of 250 µg/g. Full analytical data are provided as a supplementary data sheet.

1.3. Data processing: post-entrapment crystallization correction

Measured compositions of silicate melt inclusions and embayments were compared with bulk lava and glass geochemical trends for Cumbre Vieja using binary major element plots. Melt inclusions plot close to the observed liquid line of descent indicting that post-entrapment crystallization (PEC) of the host mineral onto the inclusion walls has had only a small effect on the measured composition.

Post-entrapment crystallization was corrected by adding equilibrium olivine back into the melt composition, assuming that the Kd value for Fe^{2+}/Mg between olivine and liquid is equal to 0.3 (Roeder and Emslie, 1970). The target Fe^{2+} for the corrected melt inclusion composition was computed as follows. Firstly, a minimum melt temperature was calculated using the measured inclusion composition and the olivine-liquid geothermometer of Helz and Thornber (1987) as modified by Putirka (2008):

$$T(°C) = 26.3 \times MgO + 994.4$$

Secondly, an inclusion trapping pressure of 522 MPa (equivalent to ~18 km depth) was assumed, consistent with microthermometry of fluid inclusions co-existing with melt inclusions in some crystals (Zanon et al., 2022). Thirdly, inclusions are assumed to be trapped at a magma oxygen fugacity of QFM+1, consistent with the mean measured oxygen fugacity of basanite melt inclusions from Lanzarote and El Hierro with measured sulfur contents between 2300 and 3700 µg/g (Moussallam et al., 2019). Fourthly, the target FeO (Fe^{2+}) and Fe_2O_3 (Fe^{3+}) contents of the PEC-corrected inclusion were calculated following the method of Kress and Carmichael (1991), under the temperature, pressure and fO_2 conditions described above. Finally, post-entrapment crystallization was corrected by adding equilibrium olivine back into the melt inclusion composition until $Kd^{ol-liq}_{Fe^{2+}-Mg}$ reached the equilibrium value of 0.3 (Roeder and Emslie, 1970). We used the Solver function in Microsoft Excel to iteratively add olivine into the inclusion until the target Kd was reached. We assume that Fe^{3+} is perfectly incompatible in olivine.

A total of 34 melt inclusions were corrected for post-entrapment crystallization. The mean correction was 1.3%, and the maximum correction was 4.9%. Seven inclusions required subtraction of equilibrium olivine to reach the target Kd, implying that small quantities of the host olivine were melted into the inclusion prior to eruption, possibly due to heating as the host crystal was entrained into the carrier melt immediately prior to eruption. The amount of olivine subtraction ranged from -0.1% to -4.6%.

Embayments are assumed to be trapped at a late stage of crystallization and therefore no PEC correction has been applied. We also measured three melt inclusions hosted in apatite, to which no PEC correction was applied.

Uncorrected and PEC-corrected melt inclusion, embayment and glass data are provided as a supplementary data sheet. Melt inclusion and embayment compositions are reported alongside the compositions of their host mineral.

Note on oxygen fugacity

A source of uncertainty in the PEC correction is the oxygen fugacity selected to calculate the target Fe^{2+}/Mg^{2+} ratio for the melt inclusion. Recent studies have documented highly oxidising conditions up to QFM+3 beneath the western Canary Islands (Taracsák et al., 2022; Nicklas et al., 2022; Day et al., 2022). To test the effect of fO_2 on the size of PEC correction, we ran multiple calculations at different oxygen fugacities for melt inclusion CAN-TLP-0040-ol4-mi1, while keeping pressure and temperature constant. For this inclusion, at an oxygen fugacity of QFM-0.15 the PEC correction required is 3.5%; at QFM+1 the PEC correction is 1.5%; and at QFM+2 the PEC correction is -

0.8% (i.e., olivine subtraction is required). These results suggest that the inclusions requiring olivine subtraction at QFM+1 may not have undergone heating, but instead that olivine subtraction may be an artefact of calculating PEC under overly oxidising conditions. However, in all cases the calculated correction is small, and does not affect the conclusions of our study.

2. Results

All melt inclusion data are available in "**Supplementary Data 1 Melt inclusion compositions.xls**". Melt inclusions, corrected for post-entrapment crystallization, contain 40.2-46.4 wt.% SiO_2, 2.8-4.5 wt.% TiO_2, 4.4-6.3 wt.% MgO and 1.1-2.1 wt.% K_2O (Fig. 1). Embayments and matrix glasses have more evolved and overlapping compositions, and contain 43.0-49.5 wt.% SiO_2, 1.4-4.1 wt.% TiO_2, 0.8-5.3 wt.% MgO and 1.0-2.9 wt.% K_2O (Fig. 1). Olivines hosting melt inclusions and embayments have compositions between Fo_{78} and Fo_{85} (Fig. 2).

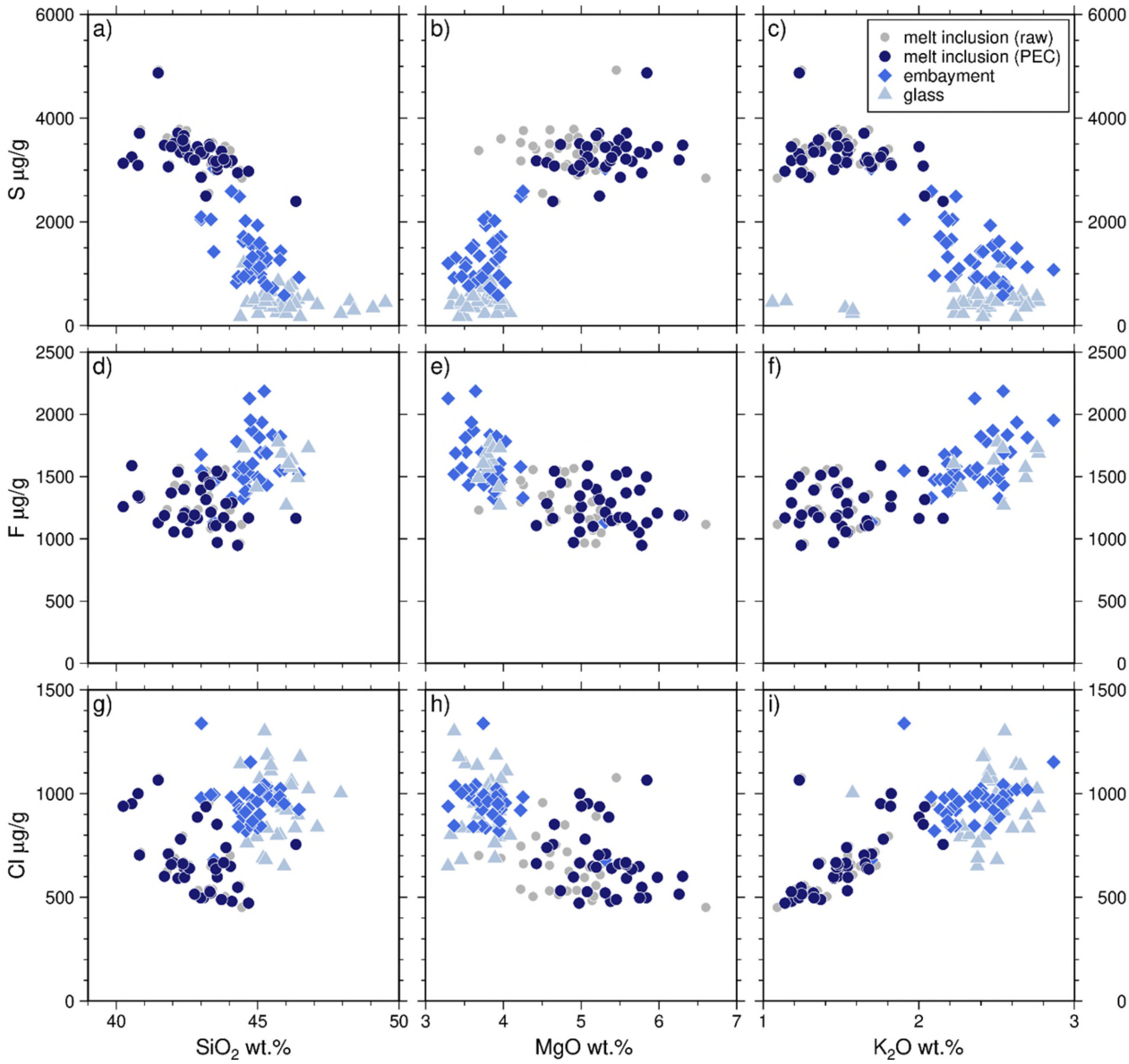

Supplementary Figure 2. Sulfur, fluorine and chlorine contents of olivine-hosted melt inclusions, embayments and matrix glasses from the 2021 Cumbre Vieja eruption. Small grey circles show measured melt inclusion compositions; dark blue symbols show melt inclusions corrected for post-entrapment crystallization. No correction is applied to embayment compositions.

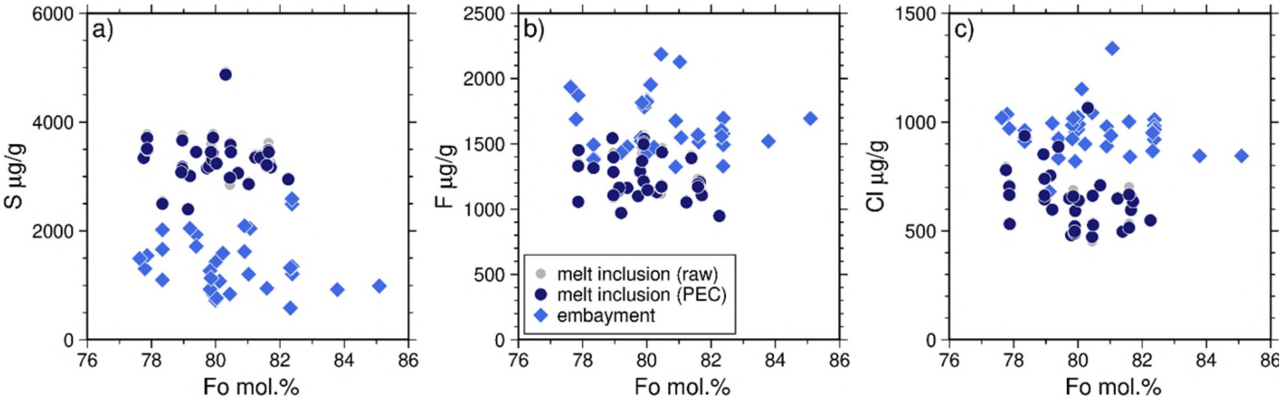

Supplementary Figure 3. Sulfur, fluorine and chlorine contents of olivine-hosted melt inclusions and embayments

versus host olivine composition for the 2021 Cumbre Vieja eruption. Small grey circles show measured melt inclusion compositions; dark blue symbols show melt inclusions corrected for post-entrapment crystallization. No correction is applied to embayment compositions.

Volatile contents of olivine-hosted melt inclusions, embayments and groundmass glasses from the 2021 Cumbre Vieja eruption. Melt inclusion compositions have been corrected for post-entrapment crystallization.

Supplementary Table 4: Melt inclusion, embayment and groundmass glass volatile contents

	Sulfur, µg/g			**Fluorine, µg/g**			**Chlorine, µg/g**		
	Mean	1σ	Range	Mean	1σ	Range	Mean	1σ	Range
Melt inclusions (PEC) *n=37*	3290	391	2396-4871	1259	169	948-1588	676	159	472-1065
Embayments *n=36*	1420	567	584-3024	1606	226	1133-2187	956	106	681-1339
Groundmass glass *n=46*	474	198	169-1207	1591	160	1269-1777	946	156	65-1301

Melt inclusion, embayment and groundmass glass volatile contents are summarized in Supplementary Figure 1 and Supplementary Table 4. The mean melt inclusion S content is 3290 µg/g. One sulfur-rich inclusion contains 4871 µg/g S, and the highest S content in the main melt inclusion population is 3715 µg/g. Groundmass glasses have a mean S content of 474 µg/g, indicating that approximately 90% of magmatic sulfur was outgassed during magma ascent and eruption.

Fluorine and chlorine become progressively more enriched as melt inclusions and glass compositions become more evolved, indicating that melt F and Cl contents are primarily governed by a fractional crystallization relationship. Embayments and groundmass glasses have similar F and Cl contents, suggesting that syn-eruptive F and Cl outgassing at the vents was inefficient.

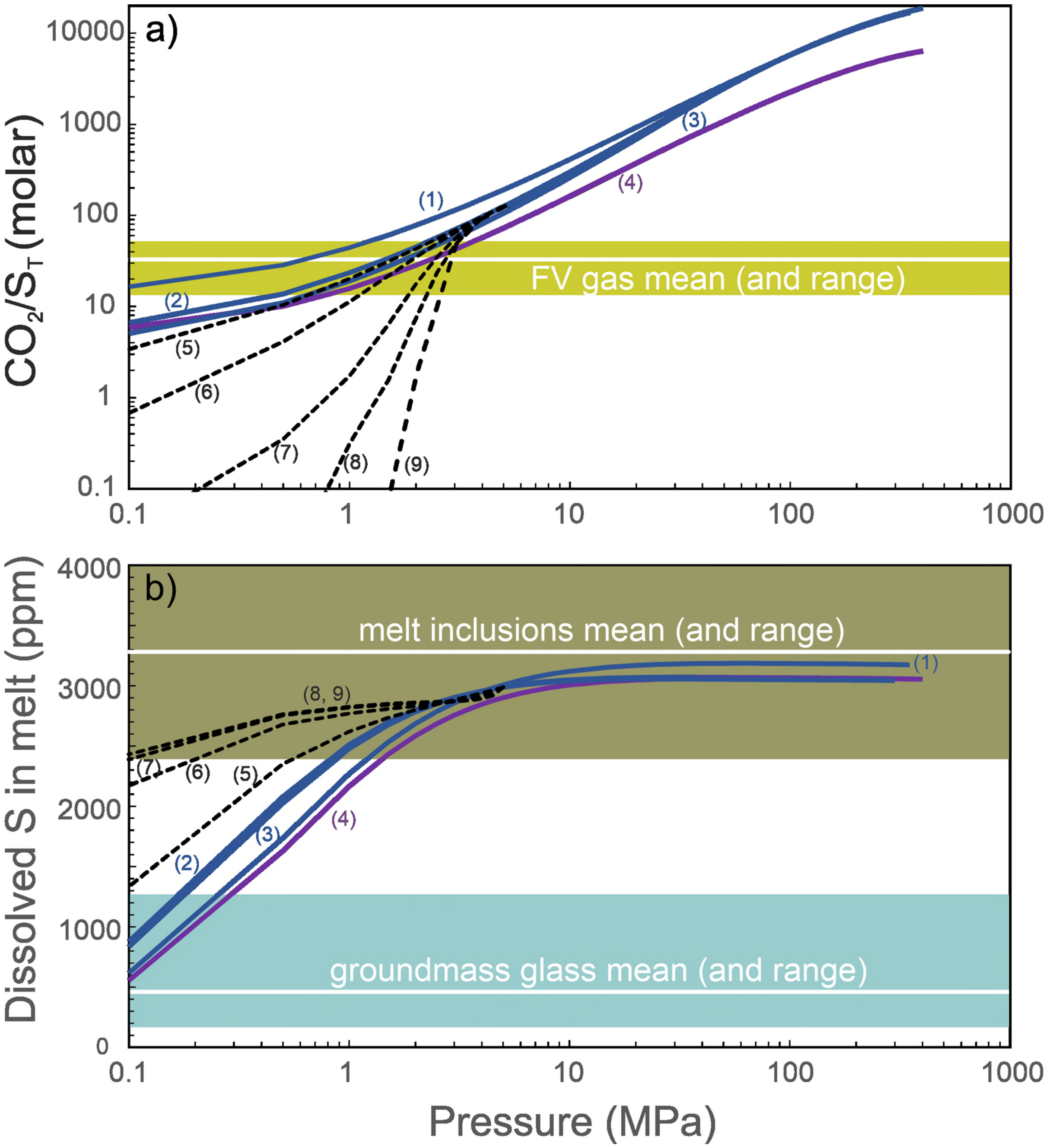

Supplementary Figure 4: (a) The gas compositions produced from different degassing pathways as described in main text figure 2; (b) Dissolved S as a function of pressure for each degassing pathway, showing also the range of melt inclusions and ground mass glass concentrations.

Supplementary Table 5 - Input parameters for degassing model runs. All runs with the Moretti et al., (2003) model. In the open system runs, gas is separated from melt during decompression, and the variable "gas fraction lost" represents the quantity (mass fraction) of gas removed at each pressure step. See Methods for details

Model run	**Degassing mode**	**Gas fraction lost**	**Initial Pressure**	**Final pressure**	**Temperature**	**Redox**	**Log fO_2**	**SiO_2**	**TiO_2**	**Al_2O_3**	**$(FeO)_T$**	**MnO**	**MgO**	**CaO**	**Na_2O**	**K_2O**	**H_2O**	**CO_2**	**S**
			(MPa)	(MPa)	(°K)	(DNNO)	bar	(wt%)	(wt%)	(wt%)	(wt%)	(wt%)	(wt%)	(wt%)	(wt%)	(wt%)	(wt%)	(wt%)	(wt%)
(1)	closed		400	0.1	1423	1	-9.3	44.3	4	14.8	12	0.19	6.6	10.9	4.3	1.9	2	5	0.3
(2)	closed		400	0.1	“”	1	-9.3	“”	“”	“”	“”	“”	“”	“”	“”	“”	“”	2	“”
(3)	closed		400	0.1	“”	1	-9.3	“”	“”	“”	“”	“”	“”	“”	“”	“”	“”	1	“”
(4)	closed		400	0.1	“”	0.5	-9.8	“”	“”	“”	“”	“”	“”	“”	“”	“”	“”	2	“”
(5)	open	0.1	5	0.1	“”	1	-9.3	“”	“”	“”	“”	“”	“”	“”	“”	“”	“”	2	“”
(6)	open	0.3	5	0.1	“”	1	-9.3	“”	“”	“”	“”	“”	“”	“”	“”	“”	“”	2	“”
(7)	open	0.5	5	0.1	“”	1	-9.3	“”	“”	“”	“”	“”	“”	“”	“”	“”	“”	2	“”
(8)	open	0.7	5	0.1	“”	1	-9.3	“”	“”	“”	“”	“”	“”	“”	“”	“”	“”	2	“”
(9)	open	0.9	5	0.1	“”	1	-9.3	“”	“”	“”	“”	“”	“”	“”	“”	“”	“”	2	“”

Supplementary Table 6 - Estimated CO_2 fluxes and parental melt CO_2 contents from Mass Eruption Rate (MER), overall SO_2 flux and different scenarios for the bulk effusion CO_2/SO_2 mass ratio, highlighted in red. Eruption rates for both 3rd October and average of the whole eruption are shown. A bulk S degassing rate of 0.30 wt.% (0.60 wt% SO2) is assumed to convert MER into effusive and explosive SO_2 flux (correcting for pre-exsolved SO_2 and partitioning between explosive and effusve branches). The degree of S exsolution prior to branching between explosive and effusive vents is set at 7.5% (see text). Mass CO_2/SO_2 ratios are then scaled to SO_2 fluxes to calculated CO_2 fluxes for both effusive, explosive and total degassing. Three scenarios are presented that differ in relative contributions from effusive/spattering degassing to the overall effusive degassing. The parental melt CO_2 content is calculated by scaling the total CO_2 flux to the total MER. Note FV is fountaining vent, EV is effusive vent and SV is the spattering vent. From this assessment, assuming 7.5% SO_2 degassing before branching, we conclude that the minimum possible initial CO2 content is 3.9 wt%, in the situation where very little relative gas flux comes from the spattering vent, the maximum CO_2 content is 5.8 wt% when all effusive degassing is sourced from the spattering vent, and the most likely scenario is no. 3, mixed emissions with overall CO_2 content of 4.5 wt%.

Degassed S at branch	7.5%		Scenario 1: Effusive vent dominated				Scenario 2: Spattering vent dominated				Scenario 3: Mixed SV and EV, best estimate			
Degassing on 3rd October			assumes average EV CO_2/SO_2 ratio of 0.1 (in mass) as representative of EV+SV degassing (e.g., the EV flux is assumed to be >> than the SV flux)				assumes average EV CO_2/SO_2 ratio of 5.0 (in mass) as representative of EV+SV degassing (e.g., the EV flux is assumed to be << than the SV flux)				assumes average EV CO_2/SO_2 ratio of 1.7 (in mass) as representative of EV+SV degassing (e.g., the EV flux is mixed with SV flux as measured with drone)			
	MER	MER proportion	CO_2/SO_2	SO_2 flux	CO_2 flux	Gas partitioning	CO_2/SO_2	SO_2 flux	CO_2 flux	Gas partitioning	CO_2/SO_2	SO_2 flux	CO_2 flux	Gas partitioning
unit	kg/s	%	mass ratio	kg/s	kg/s	%	mass ratio	kg/s	kg/s	%	mass ratio	kg/s	kg/s	%
Explosive	22600	22%	23.0	167	3852	99%	23.0	151	3471	60%	23.0	161	3695	83%
Effusive	78500	78%	0.1	436	44	1%	5.0	452	2259	38%	1.7	442	752	16%
Total	101100	100%		604	3895			603	5730			603	4448	
Parental melt CO_2 (wt %)					3.9%				5.7%				4.4%	
Degassed S at branch	7.5%		Scenario 1: Effusive vent dominated				Scenario 2: Spattering vent dominated				Scenario 3: Mixed SV and EV, best estimate			
Average degassing for whole eruption			assumes average EV CO_2/SO_2 ratio of 0.1 (in mass) as representative of EV+SV degassing (e.g., the EV flux is assumed to be >> than the SV flux)				assumes average EV CO_2/SO_2 ratio of 5.0 (in mass) as representative of EV+SV degassing (e.g., the EV flux is assumed to be << than the SV flux)				assumes average EV CO_2/SO_2 ratio of 1.7 (in mass) as representative of EV+SV degassing (e.g., the EV flux is mixed with SV flux as measured with drone)			
	MER	MER proportion	CO_2/SO_2	SO_2 flux	CO_2 flux	Gas partitioning	CO_2/SO_2	SO_2 flux	CO_2 flux	Gas partitioning	CO_2/SO_2	SO_2 flux	CO_2 flux	Gas partitioning
unit	kg/s	%	mass ratio	kg/s	kg/s	%	mass ratio	kg/s	kg/s	%	mass ratio	kg/s	kg/s	%
Explosive	20000	24%	23.0	146	3347	99%	23.0	133	3050	62%	23.0	140	3226	84%
Effusive	63000	76%	0.1	350	35	1%	5.0	363	1813	37%	1.7	355	604	16%
Total	83000	100%		496	3382			495	4863			496	3830	
Parental melt CO_2 (wt %)					4.1%				5.9%				4.6%	

Supplementary Table 7: Calculation of the dimensions and eruption rate needed to grow la Palma island, using constraints from the age of the subaerial growth (1.7 Ma) and assuming this was similar for the submarine growth. Uncertainty on total CO_2 calculation is estimated to be ~50%.

	Submarine volume		
Submarine base diameter	35	km	Mitchell et al. 2002
Submarine base area	962	km2	Guillou et al. 2001
Ocean floor depth	4	km	
Subaerial area of la palma	708	km2	
Average area	835	km2	
Estimated volume of submarine edifice	3339	km3	
	Subaerial volume		
Height of La Palma	2.423	km	
Estimated average height across island	0.85	km	
Estimated subaerial volume	602	km3	
Estimated total volume	3941	km3	
Subaerial age	1.7	Ma	
Eruption rate	354	km3/Ma	
Eruption rate	354000	m3/year	
Time to build whole edifice	11.13	Ma	
Estimated average density	2700	kg/m3	
CO_2 content	4.5	wt%	
Estimated average CO_2 emission rate/year	43011000	kg CO_2 per year	
Estimated average CO_2 emission rate/year	43011	tonnes CO_2 per year	
Estimated average CO_2 emission rate/year	0.043	Mt CO_2 per year	
Total CO_2 over 1.7 Ma (subaerial phase)	73119	Mt CO_2	
Total CO_2 over 11 Ma (lifetime)	478838	Mt CO_2	
total CO_2 over 1.7 Ma (subaerial phase)	1.66E+15	mol CO_2	
total CO_2 over 11 Ma (lifetime)	1.09E+16	mol CO_2	

Supplementary References

Day JM, Troll VR, Aulinas M, Deegan FM, Geiger H, Carracedo JC, Pinto GG, Perez-Torrado FJ (2022) Mantle source characteristics and magmatic processes during the 2021 La Palma eruption. Earth and Planetary Science Letters 597:117793, doi:10.1016/j.epsl.2022.117793

Dixon JE, Pan V (1995) Determination of the molar absorptivity of dissolved carbonate in basanitic glass. American Mineralogist 80:1339-1342, doi:10.2138/am-1995-11-1224

Guillou, H., Carracedo, J. C. & Duncan, R. A. K-Ar, 40Ar-39Ar ages and magnetostratigraphy of Brunhes and Matuyama lava sequences from La Palma Island. Journal of Volcanology and Geothermal Research 106, 175-194 (2001). https://doi.org:10.1016/s0377-0273(00)00294-8

Helz RT, Thornber CR (1987) Geothermometry of Kilauea Iki lava lake, Hawaii. Bulletin of Volcanology 49:651-668, doi:10.1007/BF01080357

Kress VC, Carmichael ISE (1991) The compressibility of silicate liquids containing Fe_2O_3 and the effect of composition, temperature, oxygen fugacity and pressure on their redox states. Contributions to Mineralogy and Petrology 108:82-92, doi:10.1007/BF00307328

Lange R, Carmichael ISE (1990) Thermodynamics properties of silicate liquids with emphasis on density, thermal expansion and compressibility. Reviews in Mineralogy 24:25-64

Mitchell, N. C., Masson, D. G., Watts, A. B., Gee, M. J. R. & Urgeles, R. The morphology of the submarine flanks of volcanic ocean islands - A comparative study of the Canary and Hawaiian hotspot islands. Journal of Volcanology and Geothermal Research 115, 83-107 (2002). https://doi.org:10.1016/s0377-0273(01)00310-9

Moore LR, Gazel E, Tuohy R, Lloyd AS, Esposito R, Steele-MacInnis M, Hauri EH, Wallace PJ, Plank T, Bodnar RJ (2015) Bubbles matter: An assessment of the contribution of vapor bubbles to melt inclusion volatile budgets. American Mineralogist 100:806-823, doi:10.2138/am-2015-5036

Moussallam Y, Longpré M-A, McCammon C, Gomez-Ulla A, Rose-Koga EF, Scaillet B, Peters N, Gennaro E, Paris R, Oppenheimer C (2019) Mantle plumes are oxidised. Earth and Planetary Science Letters 527:115798, doi:10.1016/j.epsl.2019.115798

Nicklas RW, Hahn RKM, Willhite LN, Jackson MG, Zanon V, Arevalo Jr R, Day JMD (2022) Oxidized mantle sources of HIMU-and EM-type Ocean Island Basalts. Chemical Geology 602:120901, doi:10.1016/j.chemgeo.2022.120901

Pankhurst MJ, Scarrow JH, Barbee OA, Hickey J, Coldwell BC, Rollinson GK, Rodríguez-Losada JA, Martín-Lorenzo A, Rodríguez D, Hernández W, Fernández DC, Hernández PA, Pérez NM (2022) Rapid response petrology for the opening eruptive phase of the 2021 Cumbre Vieja eruption, La Palma, Canary Islands. Volcanica 5:1-10, doi:10.30909/vol.05.01.0110

Putirka KD (2008) Thermometers and barometers for volcanic systems. Reviews in Mineralogy and Geochemistry 69:61-120, doi:10.2138/rmg.2008.69.3

Roeder PL, Emslie RF (1970) Olivine-liquid equilibrium. Contributions to Mineralogy and Petrology 29:275-289, doi:10.1007/BF00371276

Romero JE, Burton M, Cáceres F, Taddeucci J, Civico R, Ricci T, Pankhurst M, Hernandez PA, Bonadonna C, Llewellin EW, Pistolesi M, Polacci M, Solana C, D'Auria L, Arzilli F, Andronico D, Rodriguez F, Asensio-Ramos M, Hayer C, Scarlato P, Perez NM (2022) The initial phase of the 2021 Cumbre Vieja ridge eruption (Canary Islands): Products and dynamics controlling edifice growth and collapse. Journal of Volcanology and Geothermal Research 431:107642, doi:10.1016/j.jvolgeores.2022.107642

Shishkina TA, Botcharnikov RE, Holtz F, Almeev RR, Jazwa AM, Jakubiak AA (2014) Compositional and pressure effects on the solubility of H_2O and CO_2 in mafic melts. Chemical Geology 388:112-129, doi:10.1016/j.chemgeo.2014.09.001

Song Y, Chou I-M, Hu W, Burruss R, Lu W (2009) CO_2 density-Raman shift relation derived from synthetic inclusions in fused silica capillaries and its application. Acta Geologica Sinica 83:932-938, doi:10.1111/j.1755-6724.2009.00090.x

Taracsák Z, Longpré M-A, Tartèse R, Burgess R, Edmonds M, Hartley ME (2022) Highly oxidising conditions in volatile-rich El Hierro magmas: implications for ocean island magmatism. Journal of Petrology 63:egac011, doi:10.1093/petrology/egac011

Wallace PJ, Kamenetsky VS, Cervantes P (2015) Melt inclusion CO_2 contents, pressures of olivine crystallization, and the problem of shrinkage bubbles. American Mineralogist 100:787-794, doi:10.2138/am-2015-5029

Zanon V, Cyrzan K, D’Auria L, Pankhurst M, Rodríguez F, Coldwell B, Martín-Lorenzo A (2022) The magma ascent path during the 2021 eruption of Cumbre Vieja (La Palma Island, Canary archipelago) highlighted by fluid inclusions and seismicity. EGU General Assembly, doi:10.5194/egusphere-egu22-10203